Ren et al. *Zool. Res.* 2022, 43(3): 442−456
https://doi.org/10.24272/j.issn.2095-8137.2021.387

ZR | Zoological Research

Article Open Access

Characterization of two novel knock-in mouse models of syndromic retinal ciliopathy carrying hypomorphic *Sdccag8* mutations

Zhi-Lin Ren[1,2], Hou-Bin Zhang[1,2,3], Lin Li[1,2,3], Zheng-Lin Yang[1,2,3,*], Li Jiang[1,2,3,*]

[1] *Department of Laboratory Medicine*, *Sichuan Provincial People's Hospital*, *School of Medicine*, *University of Electronic Science and Technology of China*, *Chengdu*, *Sichuan* 610072, *China*

[2] *Sichuan Provincial Key Laboratory for Human Disease Gene Study*, *Sichuan Provincial People's Hospital*, *University of Electronic Science and Technology of China*, *Chengdu*, *Sichuan* 610072, *China*

[3] *Research Unit for Blindness Prevention of Chinese Academy of Medical Sciences (*2019*RU*026*)*, *Sichuan Academy of Medical Sciences*, *Chengdu*, *Sichuan* 610072, *China*

ABSTRACT

Mutations in serologically defined colon cancer autoantigen protein 8 (*SDCCAG8*) were first identified in retinal ciliopathy families a decade ago with unknown function. To investigate the pathogenesis of SDCCAG8-associated retinal ciliopathies *in vivo*, we employed CRISPR/Cas9-mediated homology-directed recombination (HDR) to generate two knock-in mouse models, *Sdccag8*$^{Y236X/Y236X}$ and *Sdccag8*$^{E451GfsX467/E451GfsX467}$, which carry truncating mutations of the mouse *Sdccag8*, corresponding to mutations that cause Bardet-Biedl syndrome (BBS) and Senior-Løken syndrome (SLS) (c.696T>G p.Y232X and c.1339–1340insG p.E447GfsX463) in humans, respectively. The two mutant *Sdccag8* knock-in mice faithfully recapitulated human SDCCAG8-associated BBS phenotypes such as rod-cone dystrophy, cystic renal disorder, polydactyly, infertility, and growth retardation, with varied age of onset and severity depending on the hypomorphic strength of the *Sdccag8* mutations. To the best of our knowledge, these knock-in mouse lines are the first BBS mouse models to present with the polydactyly phenotype. Major phototransduction protein mislocalization was also observed outside the outer segment after initiation of photoreceptor degeneration. Impaired cilia were observed in the mutant photoreceptors, renal epithelial cells, and mouse embryonic fibroblasts derived from the knock-in mouse embryos, suggesting that SDCCAG8 plays an essential role in ciliogenesis, and cilium defects are a primary driving force of SDCCAG8-associated retinal ciliopathies.

Keywords: SDCCAG8; Primary cilia; Retinal ciliopathy; Bardet-Biedl syndrome (BBS); Senior-Løken syndrome (SLS); Nephronophthisis (NPHP); Polydactyly

INTRODUCTION

Retinal ciliopathies are a group of inherited retinal degenerative diseases caused by mutations in genes

Received: 14 March 2022; Accepted: 21 April 2022; Online: 25 April 2022

Foundation items: This work was supported by the Natural Science Foundation of China (81670893, 82121003), Science and Technology Department of Sichuan Province (2021JDZH0031), and Chinese Academy of Medical Sciences (2019-I2M-5-032)

*Corresponding authors, E-mail: yangzhenglin@cashq.ac.cn; 2478639152@qq.com

encoding ciliary proteins essential for photoreceptor morphology and function (Adams et al., 2007; Bachmann-Gagescu & Neuhauss, 2019; Bujakowska et al., 2017; Chen et al., 2021). Retinal ciliopathies can present as non-syndromic retinal disorders such as Leber congenital amaurosis (LCA) or retinitis pigmentosa (RP) (Hartong et al., 2006; Koenekoop et al., 2007; Kumaran et al., 2017; Verbakel et al., 2018), as well as syndromic retinal dystrophies, such as Bardet-Biedl syndrome (BBS), Senior-Løken syndrome (SLS), Joubert syndrome (JBTS), Meckel-Gruber syndrome (MKS), Jeune syndrome, and Alström syndrome (AS) with the involvement of multiple systems and organs, including the central nervous system, kidney, skeleton, liver, and adipose tissue (Braun & Hildebrandt, 2017; Hurd & Hildebrandt, 2011; Zaghloul & Katsanis, 2009). Over 100 genes encoding retinal ciliopathy proteins are associated with retinal ciliopathies, accounting for almost 25% of all retinal dystrophies (Chen et al., 2019) (https://sph.uth.edu/retnet/).

Serologically defined colon cancer autoantigen protein 8 (*SDCCAG8*) was identified as a causative gene of retinal ciliopathy following detection of its mutation in retinal-renal ciliopathy families a decade ago (Otto et al., 2010). Genotype-phenotype correlation studies have suggested that SDCCAG8-associated syndromic ciliopathies manifest predominantly as retinal-renal degeneration, accompanied by obesity, hypogonadism, recurrent pulmonary infections, cognitive defects, and mild intellectual disability in some cases, but not with polydactyly (Halbritter et al., 2013b; Kang et al., 2016; Otto et al., 2010; Schaefer et al., 2011) (Table 1). Thus, the *SDCCAG8* gene is alternatively referred to as *NPHP10*, *SLS7*, and *BBS16*. Recent genome-wide association studies have also demonstrated that genetic polymorphisms of SDCCAG8 are associated with bipolar disorder and schizophrenia (Gonzalez et al., 2016; Hamshere et al., 2013).

The human *SDCCAG8* gene encodes a 713 residue full-length protein that contains a N-terminal globular domain (1–270 amino acids (aa)), short nuclear localization signal, and large C-terminal coiled-coil domain (CCD) (Kenedy et al., 2003; Otto et al., 2010). To date, 19 retinal ciliopathy-causing *SDCCAG8* mutations have been identified, including deletion, insertion, nonsense, and splicing mutations across exon5 to exon16 of the gene, resulting in a reading frame shift that produces C-terminal CCD-truncated proteins of different sizes (Table 1). Previous genotype-phenotype correlation studies have revealed that *SDCCAG8* truncating mutations near the N-terminal are predominantly associated with BBS, while ones near the C-terminal are primarily associated to SLS (Table 1). However, it has been difficult to correlate specific truncating mutations to phenotypic variants in SDCCAG8-associated syndromic retinal ciliopathies, and the underlying pathogenesis remains largely unknown.

Vertebrate photoreceptors possess a highly specialized primary sensory cilium, composed of a basal body (BB), connecting cilium (CC)/transition zone (TZ), and outer segment (OS), where retinal ciliopathy proteins localize and function (May-Simera et al., 2017). SDCCAG8 localizes at the BB/centrosome and CC/TZ in photoreceptors, and in other ciliated cell types in other systems, and directly interacts with other ciliopathy-associated proteins, including OFD1, NPHP5,

Table 1 SDCCAG8 mutations identified in patients with retinal ciliopathies

No.	Mutation*	Protein modification	Location of mutation	Retinal ciliopathy	References
1	421-?_740+?del (hom)	E141_R247del107fs	Exon5-7	SLS	Otto et al., 2010
2	679A>T (hom/het)	K227X	Exon7	BBS, SLS	Halbritter et al., 2013b; Otto et al., 2010
3	**696T>G (hom/het)**	Y232X	Exon7	BBS, SLS	Halbritter et al., 2013b; Otto et al., 2010
4	740_741ins741-202_741-1 (hom)	R247SfsX270 (aberrant splicing)	Intron7	BBS	Shamseldin et al., 2020
5	740+356C>T (hom)	ESE loss (aberrant splicing)	Intron7	BBS, SLS	Otto et al., 2010; Tay et al., 2020
6	740+1delG (het)	R247fsX250 (aberrant splicing)	Intron7	BBS	Otto et al., 2010
7	784G>T (het)	E262X	Exon8	SLS	Halbritter et al., 2013b
8	845_848delTTTG (hom/het)	C283X	Exon8	BBS, SLS	Kang et al., 2016; Watanabe et al., 2019; Yamamura et al., 2017
9	1068+1G>A (hom)	Aberrant splicing	Intron9	BBS	Otto et al., 2010
10	1120C>T (hom)	R374X	Exon10	BBS	Schaefer et al., 2011
11	1221+2T>A (hom)	Aberrant splicing	Intron10	BBS	Bahmanpour et al., 2021
12	1300delA (het)	N434IfsX462	Exon11	SLS	Kang et al., 2016
13	1324dupC (het)	Q442PfsX464	Exon11	SLS	Tay et al., 2020
14	**1339_1340insG (hom)**	E447GfsX463	Exon11	SLS	Otto et al., 2010
15	1420delG (hom)	E474SfsX493	Exon12	SLS	Otto et al., 2010
16	1444delA (hom/het)	T482SfsX493	Exon12	BBS, SLS	Billingsley et al., 2012; Halbritter et al., 2013b; Otto et al., 2010
17	1627_1630delGATA (het)	D543AfsX566	Exon14	BBS	Billingsley et al., 2012; Otto et al., 2010
18	1796T>G (hom)	L599X	Exon15	SLS	Otto et al., 2010
19	1946_1949delGTGT (hom)	C649SfsX658	Exon16	SLS	Otto et al., 2010

No.: Number. *: cDNA mutation numbering is based on human reference sequence NM_006642.5 for SDCCAG8, where +1 corresponds to A of ATG start translation codon. het: Heterozygous. hom: Homozygous. BBS: Bardet-Biedl syndrome. SLS: Senior-Løken syndrome.

RP1, and RPGRIP1 (Di Gioia et al., 2012; Insolera et al., 2014; Otto et al., 2010; Patil et al., 2012). Suppression of SDCCAG8 expression in zebrafish causes developmental defects in the kidney, brain, and body axis (Otto et al., 2010). *Sdccag8* mutant mouse models carrying distinct gene-trap alleles, i.e., *Sdccag8*^{gt}, *Sdccag8*$^{tm1e(EUCOMM)Wtsi}$, and *Sdccag8*^{SBT}, show loss of full-length SDCCAG8 protein expression (Airik et al., 2014; Insolera et al., 2014; Weihbrecht et al., 2018). *Sdccag8*$^{gt/gt}$ mice present with early-onset retinal degeneration, late-onset nephronophthisis (NPHP), as well as developmental and structural abnormalities of the skeleton and limbs, mimicking disease phenotypes in humans (Airik et al., 2016, 2014). In addition, the *Sdccag8*$^{tm1e(EUCOMM)Wtsi/tm1e(EUCOMM)Wtsi}$ and *Sdccag8*$^{SBT/SBT}$ mouse lines exhibit neonatal lethality with developmental defects in the central nervous system, limbs, and lungs, but without retinal-renal involvement, a major feature of SDCCAG8-assciated ciliopathies (Insolera et al., 2014; Weihbrecht et al., 2018). Thus, these three *Sdccag8* mutant mouse models show significant phenotype variation and genotype-phenotype discrepancies.

To investigate how different *SDCCAG8* truncating mutations may cause syndromic retinal ciliopathies with different severity and system involvement, we employed CRISPR/Cas9-mediated homology-directed recombination (HDR) technology to generate knock-in mouse models *Sdccag8*$^{Y236X/Y236X}$ and *Sdccag8*$^{E451GfsX467/E451GfsX467}$ carrying truncating mutations of the mouse *Sdccag8* gene, which correspond to BBS- and SLS-causing mutations in humans, respectively. Results showed that the two mutant *Sdccag8* knock-in mice closely phenocopied retinal and renal degeneration of SDCCAG8-associated retinal ciliopathies, with varying disease onset and severity. In addition, the mice displayed preaxial polydactyly, which is absent in retinal ciliopathies caused by *SDCCAG8* mutations. They also showed major phototransduction protein mislocalization outside the OS after initiation of photoreceptor death. Retinal photoreceptors, renal epithelial cells, and mouse embryonic fibroblasts (MEFs) from the knock-in mice exhibited impaired biogenesis and structural defects in cilia, suggesting that SDCCAG8 plays an essential role in ciliogenesis, and its dysfunction is an underlying mechanism driving retinal and renal degeneration in *Sdccag8* knock-in mice.

MATERIALS AND METHODS

Mutant *Sdccag8* knock-in mice

All procedures for animal experiments were approved by the Animal Care and Use Committee of Sichuan Provincial People's Hospital and conformed to the recommendations of the Association for Research in Vision and Ophthalmology (Approval No. 2014NSF(09)). Mice were maintained under 12 h cyclic dark/light conditions.

We generated two knock-in mouse models carrying either a point mutation *Sdccag8*-Y236X (c.708C>G p.Y236X) in exon7 or a 1 bp insertion *Sdccag8*-E451GfsX467 (c. 1351–1352insG p. E451GfsX467) in exon11 with CRISPR/Cas9-mediated HDR technology (Viewsolid Biotech, China). The corresponding *SDCCAG8* mutations in humans, i.e., c.696T>G p.Y232X and c.1339–1340insG p.E447GfsX463, are known to cause BBS and SLS, respectively (Otto et al., 2010). We first designed two mutation-specific guide RNA (gRNA) targets, i.e., *Sdccag8*-Y236X-g (5'-GGCTGAA ACTCACATACGAGG-3') and *Sdccag8*-E451GfsX467-g (5'-ACGTTGCGTCTCAGGAAATGG-3'), to guide sequence-specific cutting near each mutation, as well as two corresponding donor DNA oligos, i.e., *Sdccag8*-Y236X-d (5'-TCCTGCCTTGTTCTGCAGGAGAGGCTGAAACTCACATAG GATCCGGCGAAGACTGACCTTCTGGAATCTCAGCTGATG CTT-3') and *Sdccag8*-E451GfsX467-d (5'-GTCACTTAGAGGAAATTCAGAACCCGTTGCGTCTCAAGG ATCCAATGGACGTCACAAAGGTCCGAGAAAGTTTTGCTTT AA-3') to introduce the mutations into mouse *Sdccag8* genomic DNA through HDR. In addition, we designed a restriction endonuclease (BamHI) site (GGATCC) next to each mutation to facilitate mouse genotyping, as well as a synonymous mutation 1350G>A in *Sdccag8*-E451GfsX467-d to destroy the protospacer adjacent motif sequence to prevent recurrence of gRNA-mediated cutting following recombination. Each gRNA and donor DNA oligo pair was microinjected into the fertilized eggs of C57BL/6 mice together with CRISPR plasmid encoding Cas9 nuclease to generate *Sdccag8* knock-in chimeras through CRISPR/Cas9-mediated HDR. Founders with successful recombination were selected by Sanger sequencing with mouse tail DNA, and subsequently used to produce heterozygous and homozygous knock-in mice *Sdccag8*$^{Y236X/Y236X}$ and *Sdccag8*$^{E451GfsX467/E451GfsX467}$ for our study.

Mouse genotyping

Knock-in alleles *Sdccag8*-Y236X and *Sdccag8*-E451GfsX467 were identified by polymerase chain reaction (PCR) amplification with subsequent BamHI restriction enzyme digestion due to the introduction of a BamHI site next to each mutation. Two pairs of primers were designed for allele-specific PCR: i.e., *Sdccag8*-Y236X-F: ACAGCAGAGTGGAGTGAGCTAGT and *Sdccag8*-Y236X-R: TTGAGCACAGGAGACACCTAAC; *Sdccag8*-E451GfsX467-F: GCTGAGAAGGTAGAGAAGTG and *Sdccag8*-E451GfsX467-R: CACACCACACCACATACAT. PCR amplification was conducted in a total reaction volume of 20 μL. Subsequently, 8.7 μL of PCR raw products were directly digested using the BamHI restriction enzyme (New England Biolabs (NEB), USA) in a 10 μL reaction system at 37 °C for 1 h, and then analyzed by 2% agarose gel electrophoresis.

DNA constructs and transfection

We obtained pEGFP-*Sdccag8* plasmids expressing the mouse wild-type SDCCAG8 protein with the N-terminal fluorescent protein marker enhanced green fluorescent protein (EGFP) (OriGene, USA). For the generation of pEGFP-*Sdccag8* (Y236X) and pEGFP-*Sdccag8* (E451GfsX467) mutant constructs, we designed two pairs of mutagenesis primers, p*Sdccag8* (Y236X)-F: TCCGGCGAAGACTGACCTTCT and p*Sdccag8* (Y236X)-R: TCCTATGTGAGTTTCAGCCTCTC; p*Sdccag8* (E451GfsX467)-F: GATCCAATGGACGTCACAAA GGTG and p*Sdccag8* (E451GfsX467)-R: CTTGGGACGCAACGTGGTTCTGA. We then conducted QuikChange XL site-directed mutagenesis with mutagenesis

primers following the manufacturer's protocols (Stratagene, USA). The wild-type and mutant plasmids were transfected into HEK293T cells (cultured with 10% fetal bovine serum (FBS)/Dulbecco's Modified Eagle Medium (DMEM) containing 1% penicillin-streptomycin solution, 37 °C, 5% CO_2) with a Lipofectamine 3000 Kit (Invitrogen, USA). Expression of SDCCAG8 wild-type and mutant proteins in the transfected cells was analyzed by western blotting.

Preparation of MEFs

The MEFs were derived from wild-type and *Sdccag8* knock-in E13.5 embryos, as described previously (Dong et al., 2015), then cultured with 20% FBS/DMEM containing 2% penicillin-streptomycin at 37 °C in humidified 5% CO_2. To analyze cilium biogenesis, the MEFs were seeded in 24-well plates and serum-starved for 24 h before immunofluorescence staining.

Histology

The eyeballs and kidneys were dissected from euthanized (CO_2 inhalation) mice and fixed in fixative solution of 1.22% glutaraldehyde and 0.8% paraformaldehyde in 0.08 mol/L phosphate buffer at 4 °C overnight. Subsequently, the fixed tissues were dehydrated through an ethanol series and embedded in paraffin. Sections were taken at 5 μm for both retinas and kidneys. Hematoxylin and eosin staining was performed for retinal and kidney sections, and Masson trichrome staining was conducted for kidney sections following standard protocols. Images of the stained sections were acquired with a Zeiss Axiovert 200 microscope (Carl Zeiss, USA) under 63× objective. Images across the entire retinal sections were acquired with a 20× objective and imported into ImageJ v1.8.0 software with 3.8 pixels/mm scaling. The outer nuclear layer (ONL) thicknesses were measured at 500 μm intervals from the optic nerve head.

Transmission electron microscopy (TEM)

Photoreceptor ultrastructure in *Sdccag8* knock-in mice was investigated using standard protocols, as described previously (Jiang et al., 2011). Dissected mouse eyecups were first fixed in 2.5% glutaraldehyde and 1% paraformaldehyde in 0.1 mol/L cacodylate buffer overnight at 4 °C, then postfixed with 1% osmium tetroxide in 0.1 mol/L cacodylate for 1 h. The fixed eyecups were stained *en bloc* with uranyl acetate after buffer-washing and dehydrated with methanol solutions. The eyecups were subsequently embedded in Epon812 resin (Ted Pella, USA) and cut into 60 nm sections with an ultramicrotome (Leica EM UC7, Germany) near the optic nerve. The sections were placed onto carbon-coated copper grids and stained with both uranyl acetate and lead citrate for contrast enhancement. TEM was performed at 75 kV using a H-7650 electron microscope (Hitachi-Science & Technology, Japan) to observe the morphology of the photoreceptor ciliary compartments.

Western blotting

Mouse retinas and transfected cells were lysed by sonication in standard RIPA buffer (150 mmol/L NaCl, 1% Triton X-100, 0.5% sodium deoxycholate, 0.1% SDS, 50 mmol/L Tris-HCl pH 7.4) supplemented with complete protease inhibitor cocktail tablets (Roche, USA). The supernatant of protein lysates (~20 μg) was resolved using 10% sodium dodecyl-sulfate polyacrylamide gel electrophoresis (SDS-PAGE), and then transferred to a nitrocellulose membrane (0.45 μmol/L, Millipore, Germany). Subsequently, the membrane was blocked with 8% non-fat dry milk in Tris-buffered saline with 0.1% Triton X-100 (TBST) for 2 h at room temperature and then probed with primary antibodies overnight at 4 °C, followed by horseradish peroxidase (HRP)-conjugated second antibodies at room temperature for 1 h.

Immunochemistry

Mouse eyeballs were dissected from euthanized mice and immediately fixed with 4% paraformaldehyde (PFA) in 0.1 mol/L phosphate buffer (pH 7.4) for 2 h on ice, then dehydrated sequentially with 15% and 30% sucrose in 0.1 mol/L phosphate buffer (pH 7.4) for 2 h each. The eyecups were then embedded in optimal cutting temperature compound (OCT, Sakura Finetek, USA) after lens removal and cut into 12 μm retinal sections. Mouse kidneys were first dissected and fixed with 4% PFA. After dehydration with 30% sucrose for 24 h, the kidneys were embedded in OCT and cut into 5 μm sections. MEFs cultured on coverslips were fixed in 4% PFA for 10 min and permeabilized with 1% Triton X-100 for immunostaining.

For immunofluorescence staining, retinal and kidney sections, as well as MEF slides, were blocked with 10% normal donkey serum and 0.2% Triton X-100 in phosphate buffer at room temperature for 1 h, then incubated with primary antibodies overnight at 4 °C. After washing three times with phosphate buffer, the tissue sections and MEF slides were incubated with fluorescence-conjugated secondary antibodies at room temperature for 1 h. To investigate apoptosis of mouse retinas, TUNEL staining of retinal sections was performed with an *In Situ* Cell Death Detection Kit (Roche Diagnostics, China). Fluorescence images were acquired using a confocal microscope (LSM800, Carl Zeiss, Germany).

Antibodies

The primary antibodies used for western blotting and immunofluorescence analysis included: SDCCAG8 (WB 1:2 000, IHC 1:50, 13471-1-AP; Proteintech Group, USA), GRK1 (1:400, 24606-1-AP; Proteintech Group, USA), rhodopsin (1:400, 1D4, clone D4B9B; Cell Signaling Technology, CST, USA), S-opsin (1:300, Ab5407; Abcam, UK), GFP (1:3 000, 50430-2-AP; Proteintech Group, USA), GAPDH (1:5 000, 10494-1-AP; Proteintech Group, USA), β-actin (1:5 000, 20536-1-AP; Proteintech Group, USA), PDE6B (1:400, T13343; Thermo, USA), Alexa Fluor 594 conjugated peanut agglutinin (PNA) (1:200, L32459; Thermo, USA), cone arrestin (1:300, AB15282; Sigma, USA), and anti-alpha tubulin (acetyl K40) (1:1 000, ab24610; Abcam, UK). Secondary antibodies included: goat anti-rabbit Alexa Fluor 488 and 594 (1:1 000; Invitrogen, USA), goat anti-mouse Alexa Fluor 594 (1:1 000; Invitrogen, USA), and HRP-conjugated Affinipure goat anti-rabbit IgG (H+L) (1:5 000, SA00001-2; Proteintech Group, USA).

Electroretinogram (ERG) analysis

As described previously (Jiang et al., 2011), experimental

mice were dark-adapted overnight, with subsequent procedures performed under dim red light. The dark-adapted mice were first anesthetized with a combination of ketamine (16 mg/kg body weight) and xylazine (80 mg/kg body weight) by intraperitoneal injection, and their eyes were then dilated with tropicamide, phenylephrine, and tetracaine (0.5%). Body temperature was maintained at 37 °C with a heating pad. Both scotopic and photopic ERG responses were recorded from 3–5 mice with the Espion Visual Electrophysiology System (Diagnosis, AbelConn, LLC, USA). Scotopic ERG, representing rod visual function, was first conducted with light stimuli at intensities ranging from –2.52 log cd·s/m^2 to 1.30 log cd·s/m^2, while photopic ERG, representing cone visual function, was performed with light stimuli at intensities ranging from 0.48 log cd·s/m^2 to 1.30 log cd·s/m^2 after light adaptation for 20 mins. Antibiotic ointment was applied to the eyes after the ERG procedure to prevent infection.

Analysis of urine albumin to creatinine ratio (uACR)

Proteinuria, which is a major feature of chronic kidney disease (CKD), was assessed based on the uACR. We obtained 24 h urine samples from mice at P180 using metabolic cages (TSE systems, Germany). The concentrations of urine microalbumin and creatinine were measured by immunoturbidimetric assay (Mindray, China) and kinetic enzymatic assay (Maccura, China), respectively, on an AU5800 automatic biochemical analyzer (Beckman Coulter, Japan). uACR was calculated by dividing the microalbumin concentration in micrograms by the creatinine concentration in milligrams, reported as μg/mg.

Statistical analysis

T-test was used to compare data between two groups. Multiple comparisons involving more than three groups were analyzed using analysis of variance (ANOVA). Significance was determined at $P<0.05$. Data were analyzed using GraphPad Prism v8 (GraphPad Software, USA) and are presented as mean±standard error of the mean (*SEM*).

RESULTS

Generation of two knock-in mouse models expressing hypomorphic alleles, *Sdccag8*-Y236X and *Sdccag8*-E451GfsX467

Two human *SDCCAG8* recessive mutations, i.e., nonsense mutation 696T>G (p.Y232X) and 1 bp insertion 1339–1340insG (p.E447GfsX463), are known to cause syndromic retinal ciliopathies BBS and SLS, respectively (Table 1) (Otto et al., 2010). To investigate genotype-phenotype correlation and pathogenesis of SDCCAG8-associated retinal ciliopathies *in vivo*, we utilized CRISPR/Cas9-mediated HDR to generate two knock-in mouse models carrying the corresponding mouse mutations *Sdccag8*-Y236X and *Sdccag8*-E451GfsX467 (Figure 1A–C).

The knock-in mouse mutations were verified by Sanger sequencing (Figure 1D, E). To facilitate knock-in mouse genotyping, we designed a BamHI restriction site (GGATCC) adjacent to the mutations in the HDR donor oligos and performed BamHI digestion of allele-specific PCR amplificons as a routine genotyping procedure. Thus, there were two mutant allele-specific bands (258 bp and 170 bp) and one wild-type allele-specific band (425 bp) in *Sdccag8*-Y236X mouse genotyping (Figure 1F). Similarly, there were two mutant allele-specific bands (263 bp and 186 bp) and one wild-type allele-specific band (445 bp) in *Sdccag8*-E451GfsX467 mouse genotyping (Figure 1G). All three bands were present in the heterozygous mice.

Upon western blotting with anti-SDCCAG8 antibodies targeting the N-terminal epitope (1–360 aa) of SDCCAG8, we detected 27 kDa and 54 kDa truncated protein bands in $Sdccag8^{Y236X/Y236X}$ and $Sdccag8^{E451GfsX467/E451GfsX467}$ mouse retinas at P30, respectively, but the absence of the full-length SDCCAG8 protein at 83 kDa (Figure 2A). Molecular weights of the mutant proteins, SDCCAG8-Y236X and SDCCAG8-E451GfsX467, were consistent with the predicted truncations due to reading frame shift of the *Sdccag8* mutations. The expression levels of both truncated proteins were significantly decreased in the knock-in mice compared to that of the full-length protein in wild-type mice, indicating instability of the truncated proteins (Figure 2A). To confirm whether truncation and reduction of the SDCCAG8 mutant proteins could be attributed to the disease-causing mutations rather than other genetic engineering modifications via CRISPR/Cas9-mediated HDR, such as insertion of a BamHI restriction site, we expressed GFP-tagged SDCCAG8 wild-type and mutant proteins in HEK293T cells. Using immunoblotting analysis with anti-SDCCAG8 and anti-GFP antibodies, we confirmed the expression of truncated proteins in their corresponding transfected cells, consistent with the *Sdccag8* mutants expressed in *Sdccag8* knock-in mice at reduced levels (Figure 2B). To investigate the localization of truncated SDCCAG8 in mouse photoreceptors, we conducted immunochemical assays on mouse retinas at P30 (Figure 2C). SDCCAG8 was localized around the photoreceptor inner segment (IS) and CC in wild-type controls, as reported previously (Otto et al., 2010), whereas the truncated SDCCAG8 proteins were expressed in the same location in the mutant photoreceptors but with significantly deceased fluorescence signals (Figure 2C). Thus, we verified the two knock-in mouse lines carrying hypomorphic *Sdccag8* mutant alleles, $Sdccag8^{Y236X}$ and $Sdccag8^{E451GfsX467}$.

The two knock-in mouse lines displayed unexpected Mendelian ratios, with only 9.1% of $Sdccag8^{Y236X/Y236X}$ mice (40/433) and 17.4% of $Sdccag8^{E451GfsX467/E451GfsX467}$ mice (83/476) surviving after birth, significantly lower than the expected ratio of 25%. Additionally, 45% of $Sdccag8^{Y236X/Y236X}$ mice (18/40) and 42.2% of $Sdccag8^{E451GfsX467/E451GfsX467}$ mice (35/83) died within 24 h of birth. The *Sdccag8* knock-in mice had normal body size at birth but were significantly smaller than the age-matched controls at P30, indicating developmental retardation (Figure 2D). Compared to the controls (17.67±1.37 g), the $Sdccag8^{E451GfsX467/E451GfsX467}$ mice (10.50±1.38 g) and especially the $Sdccag8^{Y236X/Y236X}$ mice (9.33±1.21 g) had significantly reduced body weight (Figure 2E). Notably, all mutant males were infertile.

Development of early-onset and progressive rod-cone degeneration with varied severity in two *Sdccag8* knock-in mouse models

Previous studies have reported that individuals with

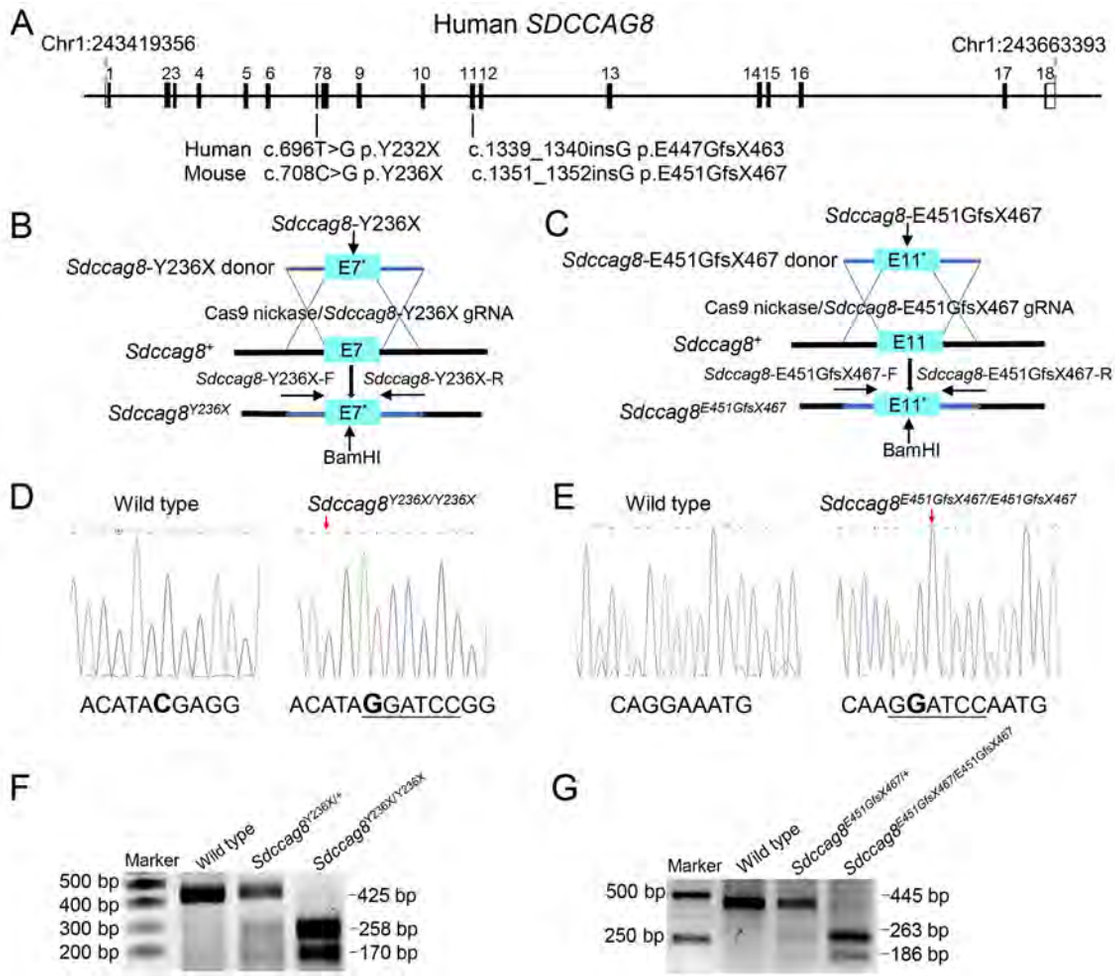

Figure 1 Generation of *Sdccag8*$^{Y236X/Y236X}$ and *Sdccag8*$^{E451GfsX467/E451GfsX467}$ knock-in mice

A: Schematic of two retinal ciliopathy-causing mutations, c.696T>G p.Y232X in exon7 and c.1339–1340insG p.E447GfsX463 in exon11, of human *SDCCAG8* gene, and corresponding mouse *Sdccag8* mutations c.708C>G p.Y236X and c.1351–1352insG p.E451GfsX467, respectively. B, C: Diagram of retinal ciliopathy-causing mutations *Sdccag8*-Y236X and *Sdccag8*-E451GfsX467 (indicated by "*") inserted in mouse *Sdccag8* gene by CRISPR/Cas9-mediated HDR with mutation-specific gRNAs and donor DNA oligos. Arrows show location of BamHI site next to each mutation and two pairs of PCR primers (*Sdccag8*-Y236X-F and -R, *Sdccag8*-E451GfsX467-F and -R) for mouse genotyping. D, E: DNA sequence traces of wild-type and two knock-in mice, *Sdccag8*$^{Y236X/Y236X}$ and *Sdccag8*$^{E451GfsX467/E451GfsX467}$, showing successful introduction of mutation 708C>G and 1351–1352insG (in bold) and BamHI restriction site (underlined). F, G: Genotyping of knock-in mice by BamHI digestion of allele-specific PCR products. *Sdccag8*-Y236X mouse genotyping (F) shows 425 bp product from wild-type allele, and 258 bp and 170 bp products from *Sdccag8*-Y236X mutant allele. *Sdccag8*-E451GfsX467 mouse genotyping (G) shows 445 bp product from wild-type allele, and 263 bp and 186 bp products from *Sdccag8*-E451GfsX467 mutant allele.

SDCCAG8-associated ciliopathies manifest early-onset and progressive retinal degeneration (Otto et al., 2010). To examine whether the *Sdccag8* knock-in mice phenocopied human retinal degeneration caused by *SDCCAG8* mutations, we performed histological analysis on mouse retinas at ages P30, P90, and P180 (Figure 3A–C). In contrast to wild-type controls with 11–12 rows of photoreceptor nuclei lining the retinal ONL, the *Sdccag8*$^{Y236X/Y236X}$ and *Sdccag8*$^{E451GfsX467/E451GfsX467}$ mice had only around six and eight rows, respectively, at P30 (Figure 3A, D). In addition, their photoreceptor OSs were about half as short as that of the wild-type controls at P30 (Figure 3A). Shortening of the ONL and OSs progressed rapidly in the knock-in mice from P30 to P180. The *Sdccag8*$^{E451GfsX467/E451GfsX467}$ mice had only around six rows of photoreceptor nuclei remaining in the ONL at P90, and close to four rows at P180 (Figure 3B–F). The *Sdccag8*$^{Y236X/Y236X}$ mice showed more severe retinal degeneration, with only four rows of photoreceptor nuclei left at P90, and two rows at P180 (Figure 3B–F). Correspondingly, their photoreceptor OSs were substantially shortened by P90 and almost completely diminished at P180, indicating rapid retinal degeneration between P30 and P180 in the knock-in mice. To examine whether the *Sdccag8* mutations also caused degeneration of cone photoreceptors, we used PNA staining, a cone specific marker, on knock-in mouse retinas at P30, P90, and P180 (Figure 3G). There was no obvious

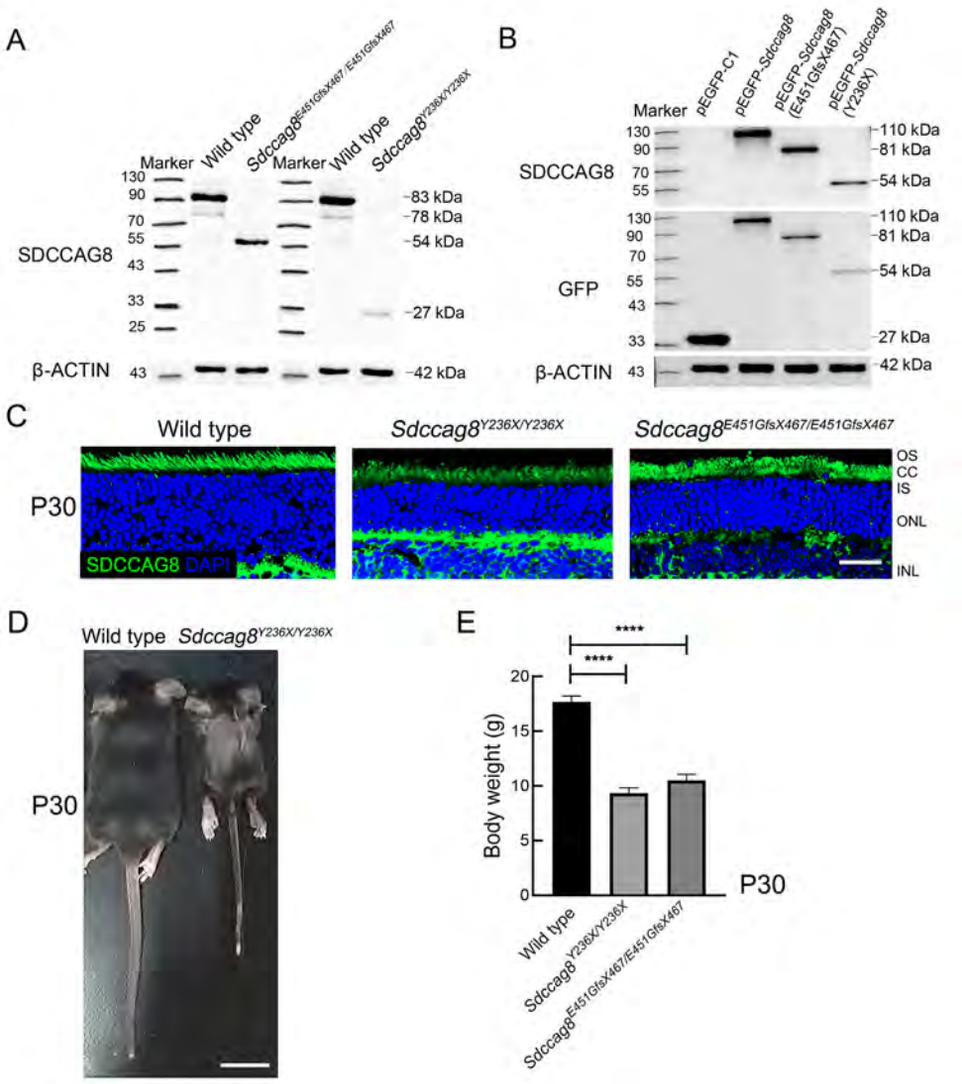

Figure 2 ***Sdccag8*** **knock-in mice carrying a hypomorphic allele with growth retardation**

A: Immunoblot of mouse retinas at P30 for SDCCAG8 showing absence of full-length 83 kDa SDCCAG8 protein. Knock-in mice show expression of a 27 kDa SDCCAG8-Y236X or 54 kDa SDCCAG8-E451GfsX467 truncated protein at different hypomorphic levels. B: Immunoblot of transfected HEK293T cells for SDCCAG8 and GFP showing expression of GFP-tagged SDCCAG8 mutant proteins, 54 kDa EGFP-SDCCAG8 (Y236X), and 81 kDa EGFP- SDCCAG8 (E451GfsX467) at different hypomorphic levels. β-actin was used as a loading control. C: Immunohistochemical analysis of mouse retinas at P30 with anti-SDCCAG8 antibody (green), showing reduced expression levels of truncated proteins at photoreceptor CCs and ISs in two knock-in mouse lines. Scale bar: 20 μm. OS, outer segment; CC, connecting cilium; IS, inner segment; ONL, outer nuclear layer; INL, inner nuclear layer. D: Representative wild-type and *Sdccag8*$^{Y236X/Y236X}$ mice at P30, revealing serious growth retardation in knock-in mice that survived to birth. Scale bar: 1 000 μm. E: Body weight analysis of wild-type and knock-in mice at P30, showing significantly reduced body weight of *Sdccag8*$^{Y236X/Y236X}$ (9.33±1.21 g, n=6) and *Sdccag8*$^{E451GfsX467/E451GfsX467}$ (10.50±1.38 g, n=6) mice compared to age-matched controls (17.67±1.37 g, n=6, ****: P<0.0001).

reduction in cone photoreceptors, even by P90, in both knock-in mice, although *Sdccag8*$^{Y236X/Y236X}$ mice showed significant loss of cones and reduced cone OS at P180, revealing late-onset cone generation in *Sdccag8* knock-in mice.

We next conducted scotopic and photopic ERGs on the knock-in mice to evaluate visual function of their rod and cone photoreceptors, respectively. For the scotopic ERGs, the a-wave amplitudes under 1.30 log cd·s/m^2 light stimuli significantly decreased by 53% in *Sdccag8*$^{Y236X/Y236X}$ mice (177.90±27.96 μV) and by 49% in *Sdccag8*$^{E451GfsX467/E451GfsX467}$ mice (192.90±31.55 μV) at P30 compared to the wild-type controls (375.50±36.36 μV) (Figure 4A–C). The scotopic ERG responses recorded from both knock-in mice declined by 78% and 69% at P90 and by 93% and 85% by P180, respectively, (Figure 4A–C). For the photopic ERGs, the b-wave amplitudes under 1.30 log cd·s/m^2 light stimuli decreased by 33% in *Sdccag8*$^{E451GfsX467/E451GfsX467}$ mice (116.40±20.58 μV) and by 38% in *Sdccag8*$^{Y236X/Y236X}$ mice (109.30±37.69 μV) at P30

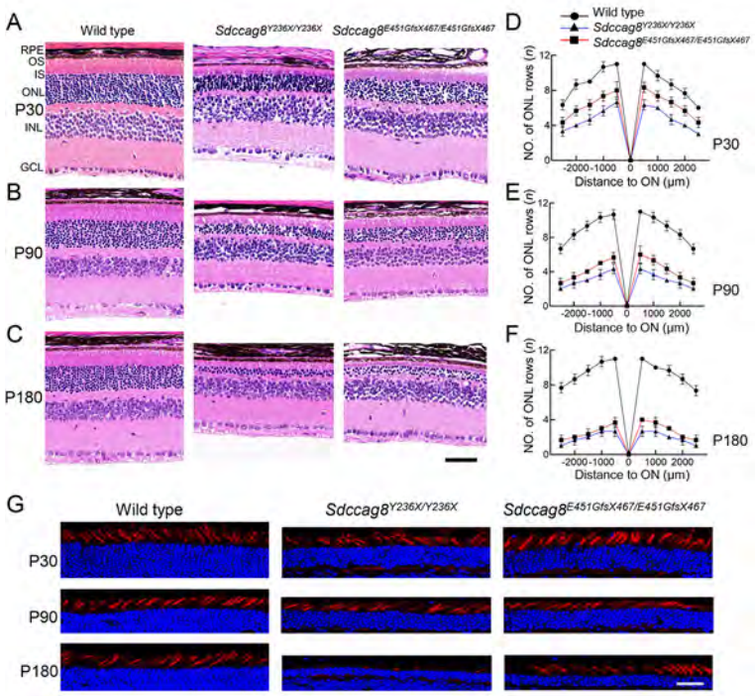

Figure 3 Retinal morphology of rod-cone photoreceptor degeneration in *Sdccag8*$^{Y236X/Y236X}$ and *Sdccag8*$^{E451GfsX467/E451GfsX467}$ knock-in mice

A–C: Histological analysis of wild-type and knock-in mouse retinas at P30 (A), P90 (B), and P180 (C) by H&E staining of retinal sections, displaying progressive shortening of ONL and OS in both knock-in mouse retinas, and noticeably earlier onset with increased severity in *Sdccag8*$^{Y236X/Y236X}$ mice. Scale bar: 20 μm. RPE, retinal pigment epithelium; OS, outer segment; IS, inner segment; ONL, outer nuclear layer; INL, inner nuclear layer; GCL, ganglion cell layer. D–F: Quantitative analysis of ONL thickness in wild-type and knock-in mouse retinas at P30, P90, and P180, showing progressive decrease in ONL thickness (nuclear number per row) in knock-in mouse retinas, which was more severe in *Sdccag8*$^{Y236X/Y236X}$ mice at all ages. Photoreceptor nuclei were counted at 500 μm increments from optic nerve. *n*=3–5. G: PNA-FITC lectin staining of wild-type and knock-in mouse retinas at P30, P90, and P180, revealing loss of cone cells initiated no earlier than P90 in both knock-in mice. Scale bar: 25 μm.

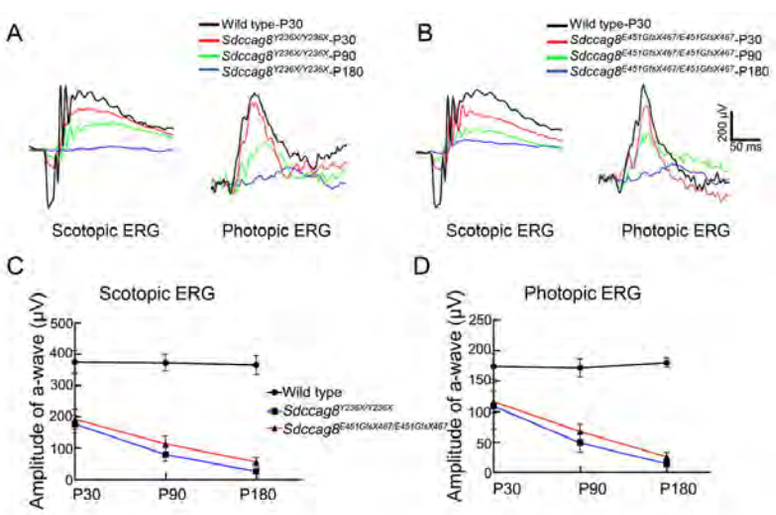

Figure 4 Scotopic and photopic electroretinograms (ERG) of rod-cone photoreceptor degeneration in *Sdccag8*$^{Y236X/Y236X}$ and *Sdccag8*$^{E451GfsX467/E451GfsX467}$ mice

A, B: Representative traces of scotopic (left) and photopic (right) ERG responses under 1.30 log cd·s/m^2 light stimuli recorded from wild-type mice at P30, as well as *Sdccag8*$^{Y236X/Y236X}$ (A) and *Sdccag8*$^{E451GfsX467/E451GfsX467}$ (B) mice at P30, P90, and P180, indicating progressive visual dysfunction of rods and cones in knock-in mice. C, D: Average a-wave amplitudes of scotopic ERG responses (C), and average b-wave amplitudes of photopic ERG responses (D) under 1.30 log cd·s/m^2 light stimuli recorded from wild-type and knock-in mice at P30, P90, and P180, revealing rapid progressive visual dysfunction of photoreceptors with earlier onset in rods. *n*=3–7.

compared to the wild-type controls (174.10±20.93 μV) (Figure 4A, B, D). Progressively, the photopic ERG responses decreased by 71% in *Sdccag8*$^{Y236X/Y236X}$ mice (49.33±15.34 μV) and 60% in *Sdccag8*$^{E451GfsX467/E451GfsX467}$ mice (66.75±12.36 μV) by P90, and further significantly declined in both knock-in mice (91% (15.33±6.01 μV) and 85% (26.67±7.17 μV), respectively) by P180 (Figure 4A, B, D), indicating that visual dysfunction caused by the *Sdccag8* mutations was more severe in *Sdccag8*$^{Y236X/Y236X}$ mice than in *Sdccag8*$^{E451GfsX467/E451GfsX467}$ mice, and was initiated earlier in rods than in cones.

Taken together, the retinal morphological and visual functional data of the knock-in mouse models demonstrated that *Sdccag8* mutations caused early-onset and rapidly progressive photoreceptor degeneration, which was more severe in *Sdccag8*$^{Y236X/Y236X}$ mice. In addition, rods degenerated earlier and faster than cones in both models, presenting as rod-cone degeneration.

Mislocalization of phototransduction proteins in *Sdccag8* mutant mouse photoreceptors

Most retinal ciliopathy-causing mutations disrupt photoreceptor morphology and function through abrogation of phototransduction cascade components, trafficking defects of the photoreceptor OS proteins, and impaired cilium biogenesis or maintenance (Bujakowska et al., 2017; Reiter & Leroux, 2017). Thus, to determine whether the *Sdccag8* truncating mutations impaired ciliary protein trafficking in photoreceptors, we first examined the localization of several membrane and membrane-associated phototransduction proteins in the knock-in mice at P30 and P90 by immunohistochemical analysis. The transmembrane protein rhodopsin was observed in the photoreceptor OS in *Sdccag8*$^{E451GfsX467/E451GfsX467}$ mice at P30 and P90, as in wild-type controls (Figure 5A, B). However, rhodopsin was mislocalized in the photoreceptor IS in *Sdccag8*$^{Y236X/Y236X}$ mice at P90, when the OS was significantly shortened (Figure 5A, B). Rhodopsin kinase (GRK1), a peripheral membrane protein involved in the phototransduction cascade, was localized in the shortened photoreceptor OS, with very little mistrafficking in the IS, ONL, and synaptic terminal in *Sdccag8*$^{Y236X/Y236X}$ and *Sdccag8*$^{E451GfsX467/E451GfsX467}$ retinas at P30 (Figure 5C). At P90, decreased mistrafficking of GRK1 was observed as the mutant photoreceptors were significantly decreased and their OSs were extensively shortened in both knock-in mice (Figure 5D). Likewise, PDE6b, another rod peripheral membrane protein, showed mistrafficking in the photoreceptors of the knock-in mice at both P30 and P90 (Figure 5E, F). Subsequently, we examined the localization of two cone phototransduction proteins in the knock-in mouse retinas, namely membrane protein S-opsin and membrane-associated protein cone arrestin, which trafficked to the cone OS in the wild-type controls. We observed remarkable mislocalization of S-opsin and cone arrestin in the cone IS and synaptic terminal in the knock-in mice at P30 and P90 (Figure 6A–D). Thus, our data revealed progressive mislocalization of OS-specific membrane proteins and membrane-associated proteins in the mutant photoreceptors, which was more obvious in the cones than in the rods.

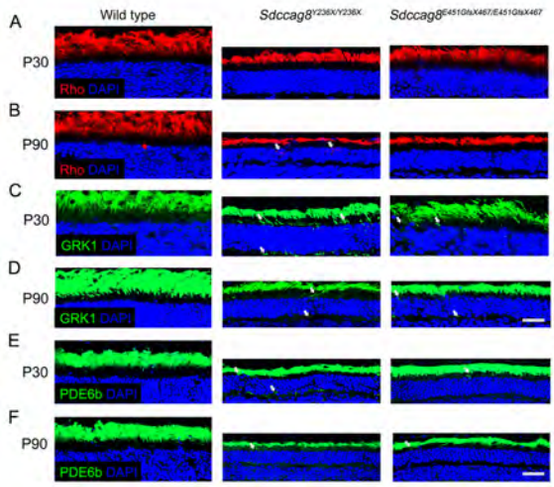

Figure 5 Immunolocalization of rod phototransduction-related proteins in *Sdccag8*$^{Y236X/Y236X}$ and *Sdccag8*$^{E451GfsX467/E451GfsX467}$ mouse retinas

Expression of membrane protein rhodopsin (A, B), as well as membrane-associated proteins rhodopsin kinase (GRK1) (C, D) and phosphodiesterase 6b (PDE6b) (E, F) in photoreceptor OS of wild-type and knock-in mouse retinas at P30 and P90, showing mislocalization of rhodopsin in photoreceptor IS and ONL in *Sdccag8*$^{Y236X/Y236X}$ retina at P90 (white arrows) and of GRK1 and PDE6b in IS, ONL, and synaptic terminals in two knock-in mouse retinas at P30 and P90 (white arrows). Scale bar: 20 μm (A–D), 25 μm (E–F).

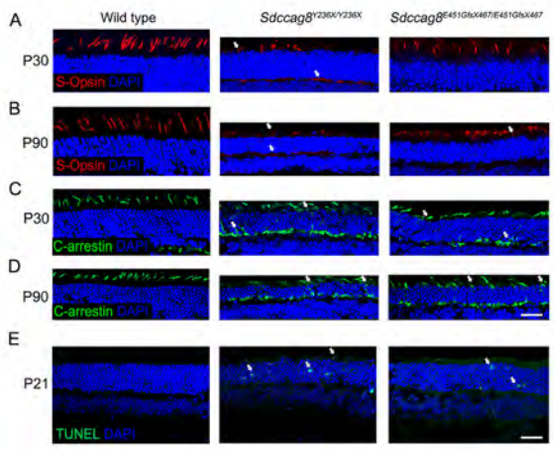

Figure 6 Immunolocalization of cone phototransduction-related proteins in *Sdccag8*$^{Y236X/Y236X}$ and *Sdccag8*$^{E451GfsX467/E451GfsX467}$ mouse retinas

A–D: Expression of membrane protein S-opsin (A, B) and membrane-associated protein C-arrestin (C, D) in wild-type and knock-in mouse retinas, showing mislocalization in cone IS, cell body, and synaptic terminals in *Sdccag8*$^{Y236X/Y236X}$ and *Sdccag8*$^{E451GfsX467/E451GfsX467}$ mice at both P30 and P90, except for S-opsin in *Sdccag8*$^{E451GfsX467/E451GfsX467}$ mice at P30. Scale bar: 20 μm. C-arrestin, Cone arrestin. E: TUNEL staining of wild-type and knock-in mouse retinas at P21, revealing early-onset photoreceptor cell death in both knock-in mice. Scale bar: 30 μm.

We subsequently tested whether protein mislocalization occurred before or after photoreceptor cell death by TUNEL staining of the knock-in mouse retinas at P21, before protein mislocalization occurred. TUNEL signals represent apoptosis, a predominant cell death mode of photoreceptor degeneration (Wright et al., 2010). We detected TUNEL signals in the ONL of both *Sdccag8*$^{Y236X/Y236X}$ and *Sdccag8*$^{E451GfsX467/E451GfsX467}$ mice at P21, but not in wild-type controls (Figure 6E), revealing that OS protein mislocalization occurred after photoreceptor cell death in the knock-in mice, probably due to shortening of the photoreceptor OS, a sink of phototransduction proteins.

Impaired photoreceptor cilia drive retinal degeneration in *Sdccag8* knock-in mice

To test whether the *Sdccag8* truncating mutations impaired photoreceptor cilia in the knock-in mice, we examined the photoreceptor ultrastructures of mutant mice at P60 by TEM, specifically focusing on the photoreceptor ciliary compartments, including BB, CC, and OS. The wild-type mice developed robust photoreceptor BB, CC, and OS compartments, with evenly stacked disk membranes (Figure 7A). In contrast, despite BB docking to photoreceptor apical membranes as usual, both *Sdccag8*$^{Y236X/Y236X}$ and *Sdccag8*$^{E451GfsX467/E451GfsX467}$ mice exhibited shortened CC and disorganized OS compartments, with significantly deteriorated disk membranes (Figure 7A). These results revealed that the structure of the photoreceptor cilia in the *Sdccag8* mutant mice was destroyed, suggesting that SDCCAG8 may function in photoreceptor cilium formation and/or maintenance.

We further studied whether the *Sdccag8* truncating mutations affected global cilium formation and maintenance by examining primary cilium formation in MEFs derived from knock-in mice (Figure 7B). We assessed cilium occurrence and length of mutant MEFs by immunofluorescence staining with an antibody against the ciliary marker acetylated tubulin after serum starvation (Figure 7B–D). Primary cilium formation

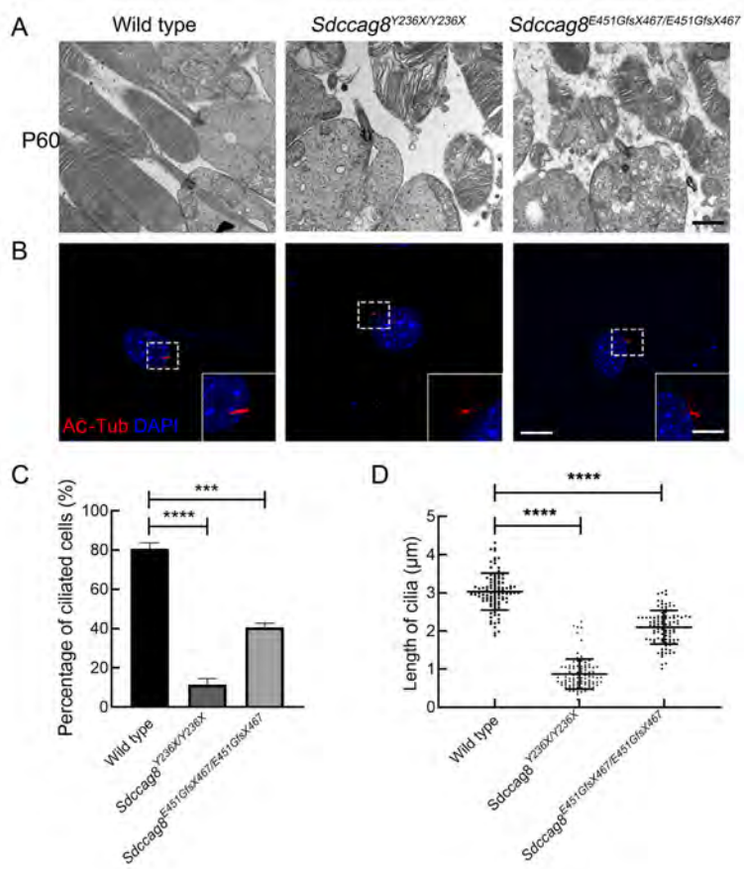

Figure 7 Impaired cilia formation in photoreceptors and MEFs from *Sdccag8*$^{Y236X/Y236X}$ and *Sdccag8*$^{E451GfsX467/E451GfsX467}$ mice

A: Photoreceptor ultrastructure of wild-type and knock-in mice at P60, demonstrating shortened CC and disorganized OS with significantly deteriorated disk membrane in dying photoreceptors of *Sdccag8*$^{Y236X/Y236X}$ and *Sdccag8*$^{E451GfsX467/E451GfsX467}$ mice. Scale bar: 1 μm. B: Immunofluorescence staining of serum-starved MEFs derived from wild-type and knock-in mice with anti-Ac-tubulin antibody (red) and nuclear dye DAPI (blue). *Sdccag8*$^{Y236X/Y236X}$ and *Sdccag8*$^{E451GfsX467/E451GfsX467}$ MEFs showed shortened cilia compared to wild-type MEFs. Scale bar: 5 μm (bottom left) and 1 μm (bottom right). C, D: Analysis of cilium formation (C) and length (D) in serum-starved MEFs derived from wild-type and knock-in mice, showing significantly reduced cilium formation in *Sdccag8*$^{Y236X/Y236X}$ (8%) and *Sdccag8*$^{E451GfsX467/E451GfsX467}$ (39%) MEFs, with decreased cilium lengths of 0.87±0.39 μm and 2.09±0.44 μm, respectively. In contrast, ~80% of wild-type MEFs grew cilia with an average length of 3.03±0.48 μm. n=100 for each genotype, ***: P<0.001; ****: P<0.0001.

was only found in 8% (8/100) of *Sdccag8*$^{Y236X/Y236X}$ MEFs and 39% (39/100) of *Sdccag8*$^{E451GfsX467/E451GfsX467}$ MEFs, in contrast to 80% (80/100) of wild-type control MEFs (Figure 7C). Additionally, the average lengths of cilia in the *Sdccag8*$^{Y236X/Y236X}$ and *Sdccag8*$^{E451GfsX467/E451GfsX467}$ MEFs were 0.87 μm and 2.10 μm, respectively, significantly shorter than that of the controls (Figure 7B, D). These results suggest that SDCCAG8 is essential for global cilium formation.

Our results revealed that impaired photoreceptor ciliary structure is a primary pathogenic force driving photoreceptor degeneration in the knock-in mice, with SDCCAG8 implicated to play a critical role in photoreceptor ciliary formation and maintenance, rather than ciliary protein trafficking.

Nephronophthisis and defective epithelial cilia in *Sdccag8* knock-in mice

Patients with SDCCAG8-associated ciliopathies and *Sdccag8*$^{gt/gt}$ gene-trap mice with loss of *Sdccag8* function exhibit NPHP, a renal cystic disease characterized by corticomedullary cysts, tubular basement membrane disruption, and tubulointerstitial nephropathy in renal histology (Stokman et al., 2016). Thus, we investigated whether the knock-in mice developed NPHP.

We observed kidney enlargement in *Sdccag8*$^{Y236X/Y236X}$ mice as early as P30, and the mutant kidneys became progressively larger at P90 and deformed at P180 (Figure 8A). Correspondingly, small cysts formed in the cortical region of the *Sdccag8*$^{Y236X/Y236X}$ mice at P30, as visualized by renal histological assay (Figure 8B). From P90 to P180, the *Sdccag8*$^{Y236X/Y236X}$ mouse kidneys progressively deteriorated, with renal cysts spreading beyond the cortical region to the corticomedullary junction, cortical cysts becoming enlarged, and renal parenchyma replaced by interstitial infiltrates (Figure 8B). However, different from early-onset NPHP in *Sdccag8*$^{Y236X/Y236X}$ mice, no shape change or cyst formation was detected in the *Sdccag8*$^{E451GfsX467/E451GfsX467}$ mouse kidneys at P30 (Figure 8A, B). Relatively mild kidney enlargement and cyst formation in the kidney cortical region were observed in the *Sdccag8*$^{E451GfsX467/E451GfsX467}$ mice at P90 to P180 (Figure 8A, B). To examine renal fibrosis in the knock-in mice, we performed Masson trichrome staining of renal sections. Consistent with histology, the *Sdccag8*$^{Y236X/Y236X}$ mice showed rapidly progressive renal fibrosis, from mild fibrosis surrounding the dilated tubules at P30 and P90 to extensive collagen deposits distributed across the renal tissue at P180 (Figure 8C). Renal fibrosis was not detected in the *Sdccag8*$^{E451GfsX467/E451GfsX467}$ mouse kidneys at P30 but was observed minimally at P90 and obviously at P180 (Figure 8C). Thus, our data demonstrated that NPHP occurred in both knock-in mouse models but with different severities and

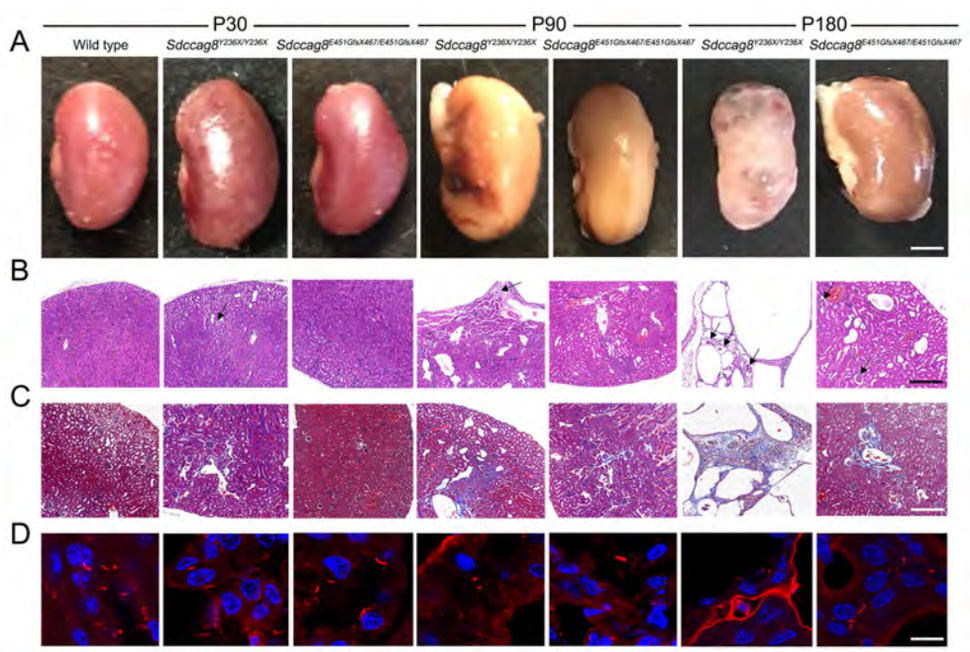

Figure 8 Nephronophthisis in *Sdccag8*$^{Y236X/Y236X}$ and *Sdccag8*$^{E451GfsX467/E451GfsX467}$ mice accompanied by defective renal cilia

A: Representative kidneys dissected from wild-type and knock-in mice at P30, P90, and P180, showing moderate enlargement and deformation of kidneys in *Sdccag8*$^{Y236X/Y236X}$ and *Sdccag8*$^{E451GfsX467/E451GfsX467}$ mice. Scale bar: 1 000 μm. B: H&E staining of kidney sections from wild-type and knock-in mice at P30, P90, and P180, displaying progressive development of tubular cysts and interstitial infiltrates in kidneys from both knock-in mice. Phenotype presented earlier and more severely in *Sdccag8*$^{Y236X/Y236X}$ mouse kidneys than in *Sdccag8*$^{E451GfsX467/E451GfsX467}$ kidneys. Black arrows indicate glomerular cysts. Scale bar: 100 μm. C: Masson trichrome staining of wild-type and knock-in mouse kidneys at P30, P90, and P180, revealing more severe renal fibrosis in *Sdccag8*$^{Y236X/Y236X}$ mouse kidneys, and milder fibrosis in *Sdccag8*$^{E451GfsX467/E451GfsX467}$ kidneys at P90 and P180. Scale bar: 100 μm. D: Immunohistochemical analysis of renal cilium formation in knock-in mice at P30, P90, and P180 with anti-acetylated tubulin (Ac-Tub) antibodies, showing progressive impairment of renal cilia in *Sdccag8*$^{Y236X/Y236X}$ and *Sdccag8*$^{E451GfsX467/E451GfsX467}$ mice. Scale bar: 2 μm.

progressed in concert with photoreceptor degeneration.

We next tested the uACR to investigate whether the knock-in mice developed CKD, a typical clinical feature of NPHP and precursor to end-stage renal disease (ESRD). The uACR is a sensitive and specific surrogate marker for proteinuria, indicating progression of CKD (Hildebrandt et al., 2009). We collected 24 h urine samples from three P180 mice for each knock-in model and analyzed the uACR with an automatic biochemical analyzer. The 24 h uACRs in *Sdccag8*$^{Y236X/Y236X}$ (132.5±7.0 μg/mg) and *Sdccag8*$^{E451GfsX467/E451GfsX467}$ (59.4±7.0 μg/mg) mice were significantly elevated (3.3 and 1.5 times, respectively) compared to the wild-type controls (39.6±5.4 μg/mg). The uACR results indicated CKD progression in both knock-in mice by P180, with increased severity in *Sdccag8*$^{Y236X/Y236X}$ mice.

We next investigated whether the *Sdccag8* mutations affected biogenesis of cilia in the mouse kidneys, similar to their effects on photoreceptors and MEFs. Renal cilia were examined by staining kidney sections with an antibody against the cilium marker acetylated tubulin. The number and length of renal epithelial cilia were significantly decreased in the distal convoluted tubules and cortical collecting ducts of the *Sdccag8*$^{E451GfsX467/E451GfsX467}$ kidneys and were completely absent in the *Sdccag8*$^{Y236X/Y236X}$ kidneys (Figure 8D).

Taken together, our data demonstrate that the knock-in mice carrying *Sdccag8* truncating mutations displayed NPHP and developed CKD, with earlier onset and increased severity in *Sdccag8*$^{Y236X/Y236X}$ mice. The ciliary defects detected in the kidney epithelial cells may be a driving force of renal cyst formation in *Sdccag8* knock-in mice.

Hind limb preaxial polydactyly in *Sdccag8* knock-in mice

Postaxial polydactyly is a major clinical feature of BBS in humans. Thus, we examined whether this phenotype was present in the knock-in mouse models. Interestingly, the mutant mice exhibited preaxial polydactyly of the hind limbs, with 100% (40/40) penetrance in the *Sdccag8*$^{Y236X/Y236X}$ mice and 95% (79/83) penetrance in the *Sdccag8*$^{E451GfsX467/E451GfsX467}$ mice (Figure 9A, B). Bilateral polydactyly was predominant, accounting for 80% (32/40) of the *Sdccag8*$^{Y236X/Y236X}$ mice and 58% (48/83) of the *Sdccag8*$^{E451GfsX467/E451GfsX467}$ mice (Figure 9B). Among the mice with unilateral polydactyly, 75% (6/8) of the *Sdccag8*$^{Y236X/Y236X}$ mice and 65% (20/31) of the *Sdccag8*$^{E451GfsX467/E451GfsX467}$ mice presented with right-sided polydactyly, significantly more than left-sided polydactyly (Figure 9B). The development of polydactyly as a ciliopathy phenotype in the mouse models is consistent with previous findings in three gene-trap mouse models (Airik et al., 2016; Insolera et al., 2014; Weihbrecht et al., 2018), supporting the hypothesis that SDCCAG8 participates in digit development in mice.

DISCUSSION

In this study, two novel *Sdccag8* knock-in mouse lines *Sdccag8*$^{Y236X/Y236X}$ and *Sdccag8*$^{E451GfsX467/E451GfsX467}$, each carrying a distinct hypomorphic allele, were generated by CRISPR/Cas9-HDR. They faithfully recapitulated human SDCCAG8-associated BBS phenotypes with varied phenotypic age of onset and severity, which were directly

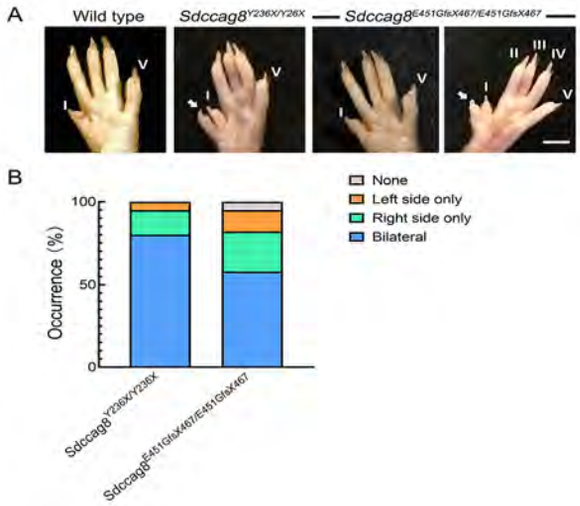

Figure 9 Preaxial polydactyly phenotype in *Sdccag8*$^{Y236X/Y236X}$ and *Sdccag8*$^{E451GfsX467/E451GfsX467}$ mice

A: Representative images of hind limbs of wild-type and knock-in mice, demonstrating preaxial polydactyly in hind limbs in *Sdccag8*$^{Y236X/Y236X}$ and *Sdccag8*$^{E451GfsX467/E451GfsX467}$ mice, with 95%–100% penetrance. Digits are marked with Roman numerals from I to V starting from the thumb. Scale bar: 2 000 μm. B: Variable preaxial polydactyly phenotypes in knock-in mice, with predominance of bilateral polydactyly accounting for ~80% and 58% in *Sdccag8*$^{Y236X/Y236X}$ and *Sdccag8*$^{E451GfsX467/E451GfsX467}$ mice, respectively.

proportional to the hypomorphic strength of the *Sdccag8* mutations, Y236X and E451GfsX467. To the best of our knowledge, these knock-in mice were the first BBS mouse models to present with polydactyly. Impaired cilia were observed in the mutant photoreceptors, renal epithelial cells, and MEFs derived from the knock-in mouse embryos. Therefore, we propose that cilium defects are the primary driving force of SDCCAG8-associcated BBS in humans.

Due to a pivotal role of cilia in diverse cellular processes of embryonic and postnatal development (Reiter & Leroux, 2017), most ciliopathy-associated mutations identified in humans are hypomorphic, including *Sdccag8* mutations, resulting in prenatal developmental defects, as well as clinical manifestations arising after birth. Thus, it is unsurprising that complete loss of a ciliopathy-associated gene is devastating to mice and humans (Norris & Grimes, 2012). Two out of three *Sdccag8* mutant mice previously generated by gene trap show embryonic lethality, with developmental defects in the central nervous system, limbs, and lungs, but without primary features of SDCCAG8-assciated ciliopathies, i.e., retinal and renal defects (Insolera et al., 2014; Weihbrecht et al., 2018). Therefore, conventional genetic modification approaches to generate null alleles may not be appropriate for modeling ciliopathy-associated diseases. The generation of hypomorphic alleles with a range of strengths for diseases that explicitly model human ciliopathies can be technically demanding (Rix et al., 2011). Among current genome engineering technologies, the CRISPR/Cas9 system is a programmable nuclease-based genome-editing technology that enables highly efficient and precise modification of a

variety of eukaryotic and mammalian species (Banan, 2020; Hsu et al., 2014). Employing CRISPR/Cas9-HDR in this study, we successfully developed two mouse models carrying hypomorphic alleles of *Sdccag8*, which closely mimicked human BBS with phenotypic variation.

The mouse *Sdccag8* mutations *Sdccag8*-Y236X and *Sdccag8*-E451GfsX467 respectively correspond to BBS- and SLS-causing mutations in humans (Halbritter et al., 2013a; Otto et al., 2010). The corresponding knock-in mice generated in this study lacked the full-length SDCCAG8 protein and showed significantly decreased expression of the specific truncated proteins, in contrast to the null alleles described in three previously generated *Sdccag8* gene-trap mice (Airik et al., 2014; Insolera et al., 2014; Weihbrecht et al., 2018). The fewer truncated proteins could be attributed to nonsense mediated decay due to the inclusion of an early stop codon in the *Sdccag8* mutant alleles. Previous genetic studies have suggested that only the full-length isoform SDCCAG8-a is relevant for the retinal-renal phenotype of SDCCAG8-associated ciliopathies, with specific expression in the photoreceptor CC and ISs of mouse retinas (Otto et al., 2010). The mutants *SDCCAG8*-Y236X and *SDCCAG8*-E451GfsX467 caused different-sized truncations of the C-terminal CCD. Notably, based on immunochemical analysis of the knock-in mouse retinas, SDCCAG8-Y236X exhibited weaker fluorescence signals than SDCCAG8-E451GfsX467 in the mutant photoreceptor CC and ISs, suggesting that the size of the truncated CCD was directly proportional to the hypomorphic strength of the mutations.

Histological and ERG analysis of mouse retinas showed early-onset and rapidly progressive rod-cone photoreceptor degeneration in the *Sdccag8* knock-in mice. Retinal degenerative changes, including photoreceptor ONL and OS shortening, were observed in the $Sdccag8^{Y236X/Y236X}$ mice as early as P30, and rapidly progressed to almost complete deterioration within 6 months. The $Sdccag8^{E451GfsX467/E451GfsX467}$ mice showed less severe morphological and functional changes in photoreceptor degeneration, progressing about one month later than the $Sdccag8^{Y236X/Y236X}$ mice. In addition, loss of cone photoreceptors was first observed in mutant retinas at P180, and ERG responses from cones decreased by ~20% in the knock-in mice at P30. In contrast, a 35%–50% loss of rods and 50% decrease in ERG responses from rods were observed in the knock-in mice even at P30. Thus, late-onset cone death and dysfunction revealed rod-cone photoreceptor degeneration in SDCCAG8-associated retinal ciliopathies.

In addition, early- and late-onset NPHP developed in the two knock-in mouse models, respectively, with formation of renal cysts in $Sdccag8^{Y236X/Y236X}$ mice as early as P30, but at P90 in $Sdccag8^{E451GfsX467/E451GfsX467}$ mice. However, among the three previously generated *Sdccag8* gene-trap mouse models, only $Sdccag8^{gt/gt}$ mice exhibited late-onset NPHP, with embryonic lethality reported in the other mice (Airik et al., 2014; Insolera et al., 2014; Weihbrecht et al., 2018). NPHP is a cystic renal disease that constitutes the most frequent genetic cause of ESRD in children and young adults, and is characterized by corticomedullary cysts, tubular basement membrane disruption, and tubulointerstitial nephropathy in renal histology (Stokman et al., 2016). The *Sdccag8* knock-in mice displayed moderately enlarged and/or deformed kidneys, not unlike infantile NPHP in humans (Airik et al., 2014; Braun & Hildebrandt, 2017; Kang et al., 2016; Otto et al., 2010). Previous mouse models of cystic renal disease have shown renal cysts in the cortical region during the early stages, with spread to the corticomedullary junction and interstitial infiltrates at the end stage (Atala et al., 1993; Attanasio et al., 2007). Similarly, our mouse models demonstrated renal fibrosis surrounding dilated tubules during early disease, and later widespread deterioration of renal tissue. Here, mouse renal function was evaluated by 24 h uACR testing, which indicated excessive proteinuria in $Sdccag8^{Y236X/Y236X}$ mice at P180, consistent with ESRD. The different severities of NPHP in the two knock-in mouse models further demonstrated the different hypomorphic strengths of the *Sdccag8*-Y236X and *Sdccag8*-E451GfsX467 mutant alleles.

The three previously reported *Sdccag8* gene-trap mouse lines exhibit preaxial polydactyly penetrance of 65%–100% (Airik et al., 2016; Insolera et al., 2014; Weihbrecht et al., 2018), similar to the two knock-in mouse lines at 95% and 100%, respectively. As an embryonically developed phenotype, polydactyly is a primary feature of BBS and other ciliopathies, such as MKS, JBTS, orofaciodigital syndrome (OFD), and McKusick-Kaufman syndrome (MKKS), but not SLS (Zaghloul & Katsanis, 2009). About 79% of BBS patients present with postaxial polydactyly, but the polydactyly phenotype is absent in human SDCCAG8-assciated ciliopathies (Beales et al., 1999; Forsythe & Beales, 2013; Otto et al., 2010; Schaefer et al., 2011). To the best of our knowledge, the *Sdccag8*-associated mutant mice, including the gene-trap and knock-in mice, are the first BBS mouse models characterized by digital malformation. In addition, instead of presenting postaxial polydactyly on any limb, as seen in BBS patients, the *Sdccag8*-associated mouse models exhibited preaxial polydactyly on hind limbs only. Many ciliary gene mutations causing polydactyly are attributed to disruption of the Sonic Hedgehog (Shh) signaling pathway, which requires the presence of intact primary cilia for activation (Zaghloul & Katsanis, 2009). The presence of polydactyly in the knock-in mice suggests that SDCCAG8 is necessary for cilium biogenesis and/or maintenance of the developing limb bud in mice, but not in humans. Furthermore, this suggests species-specific differences in Shh-dependent determination of digit number and identity. Therefore, further studies are needed to improve our understanding of the underlying pathogenesis of polydactyly in human BBS.

The two *Sdccag8* knock-in mouse lines were characterized as BBS animal models, displaying four out of the six BBS primary manifestations, including rod-cone dystrophy, cystic renal disorder, polydactyly, and male infertility, as well as secondary developmental delay. Phenotypic severity and age of onset were dependent on the hypomorphic strength of the *Sdccag8* mutations, which was directly correlated to truncation size and expression level of the mutant alleles.

We also explored the pathogenesis of SDCCAG8 mutation-causing retinal ciliopathies by dissecting OS protein trafficking and ciliary structure of the mutant photoreceptors in the *Sdccag8* knock-in mice. We discovered rod

phototransduction-related proteins, including rhodopsin, GRK1, and PDE6, localized not only in the OS, but also in the photoreceptor IS, ONL, and/or synaptic terminals of the knock-in mice at P90, when rod photoreceptors were dying and their OSs were significantly shortened. In addition, cone phototransduction-related proteins S-opsin and cone arrestin were significantly mislocalized in the IS, ONL, and synaptic terminals at P30, which was probably due to differences in OS biogenesis or protein trafficking between cones and rods (Anderson et al., 1978; Eckmiller, 1987). However, based on TUNEL staining, we found that photoreceptor cell death occurred earlier than OS protein mislocalization in the mutant photoreceptors, suggesting that *Sdccag8* mutation-causing protein mislocalization occurred after photoreceptor cell death. Impaired ciliary structures, including shortened CC and disrupted OS, were detected in the knock-in mice by TEM analysis of retinas. Impaired renal epithelial cilia were observed in the distal convoluted tubules and cortical collecting ducts of the mutant kidneys. In addition, *Sdccag8* mutation-causing global cilium defects were verified in MEFs derived from the knock-in mice. Thus, our data demonstrated that cilium defects were a primary force driving BBS phenotypes in the knock-in mice, suggesting that SDCCAG8 plays an essential role in biogenesis and maintenance of cilia in multiple systems during embryonic development and after birth. Notably, we found that SDCCAG8 is a ciliary protein involved in retinal ciliopathies and plays a key role in cilium assembly and/or maintenance. Further analysis of its role should provide insights into ciliary function and increase our understanding of the signaling, physiological, and developmental functions of cilia.

COMPETING INTERESTS

The authors declare that they have no competing interests.

AUTHORS' CONTRIBUTIONS

L.J. and Z.L.Y. designed the study and wrote and revised the manuscript. Z.L.R. performed the experiments, analyzed the data, and drafted the manuscript. H.B.Z. and L.L. helped analyze the data and reviewed and edited the manuscript. All authors read and approved the final version of the manuscript.

ACKNOWLEDGEMENTS

We thank Shu-Jin Li, Mu Yang, and Shan-Shan Zhang for assistance in the immunochemical experiments and Jia-Liang Yang and Zhi-Lin Jiang for assistance in the ERG experiment. We also thank Lin Wang for help in breeding mice and Tian-Ge Song and Ke-Cheng Li for help in obtaining tail clips from mice.

REFERENCES

Adams NA, Awadein A, Toma HS. 2007. The retinal ciliopathies. *Ophthalmic Genetics*, **28**(3): 113−125.

Airik R, Schueler M, Airik M, Cho J, Ulanowicz KA, Porath JD, et al. 2016. SDCCAG8 interacts with RAB effector proteins RABEP2 and ERC1 and is required for hedgehog signaling. *PLoS One*, **11**(5): e0156081.

Airik R, Slaats GG, Guo Z, Weiss AC, Khan N, Ghosh A, et al. 2014. Renal-retinal ciliopathy gene *Sdccag8* regulates DNA damage response signaling. *Journal of the American Society of Nephrology*, **25**(11): 2573−2583.

Anderson DH, Fisher SK, Steinberg RH. 1978. Mammalian cones: disc shedding, phagocytosis, and renewal. *Investigative Ophthalmology & Visual Science*, **17**(2): 117−133.

Atala A, Freeman MR, Mandell J, Beier DR. 1993. Juvenile cystic kidneys (*jck*): a new mouse mutation which causes polycystic kidneys. *Kidney International*, **43**(5): 1081−1085.

Attanasio M, Uhlenhaut NH, Sousa VH, O'Toole JF, Otto E, Anlag K, et al. 2007. Loss of GLIS2 causes nephronophthisis in humans and mice by increased apoptosis and fibrosis. *Nature Genetics*, **39**(8): 1018−1024.

Bachmann-Gagescu R, Neuhauss SC. 2019. The photoreceptor cilium and its diseases. *Current Opinion in Genetics & Development*, **56**: 22−33.

Bahmanpour Z, Daneshmandpour Y, Kazeminasab S, Khalil Khalili S, Alehabib E, Chapi M, et al. 2021. A novel splice site mutation in the SDCCAG8 gene in an Iranian family with Bardet-Biedl syndrome. *International Journal of Ophthalmology*, **41**(2): 389−397.

Banan M. 2020. Recent advances in CRISPR/Cas9-mediated knock-ins in mammalian cells. *Journal of Biotechnology*, **308**: 1−9.

Beales PL, Elcioglu N, Woolf AS, Parker D, Flinter FA. 1999. New criteria for improved diagnosis of Bardet-Biedl syndrome: results of a population survey. *Journal of Medical Genetics*, **36**(6): 437−446.

Billingsley G, Vincent A, Deveault C, Heon E. 2012. Mutational analysis of SDCCAG8 in Bardet-Biedl syndrome patients with renal involvement and absent polydactyly. *Ophthalmic Genetics*, **33**(3): 150−154.

Braun DA, Hildebrandt F. 2017. Ciliopathies. *Cold Spring Harbor Perspectives in Biology*, **9**(3): a028191.

Bujakowska KM, Liu Q, Pierce EA. 2017. Photoreceptor cilia and retinal ciliopathies. *Cold Spring Harbor Perspectives in Biology*, **9**(10): a028274.

Chen HY, Kelley RA, Li TS, Swaroop A. 2021. Primary cilia biogenesis and associated retinal ciliopathies. *Seminars in Cell & Developmental Biology*, **110**: 70−88.

Chen HY, Welby E, Li TS, Swaroop A. 2019. Retinal disease in ciliopathies: recent advances with a focus on stem cell-based therapies. *Translational Science of Rare Diseases*, **4**(1-2): 97−115.

Di Gioia SA, Letteboer SJF, Kostic C, Bandah-Rozenfeld D, Hetterschijt L, Sharon D, et al. 2012. FAM161A, associated with retinitis pigmentosa, is a component of the cilia-basal body complex and interacts with proteins involved in ciliopathies. *Human Molecular Genetics*, **21**(23): 5174−5184.

Dong SL, Maziveyi M, Alahari SK. 2015. Primary tumor and MEF Cell Isolation to Study Lung Metastasis. *Journal of Visualized Experiments*, (99): e52609.

Eckmiller MS. 1987. Cone outer segment morphogenesis: taper change and distal invaginations. *Journal of Cell Biology*, **105**(5): 2267−2277.

Forsythe E, Beales PL. 2013. Bardet–Biedl syndrome. *European Journal of Human Genetics*, **21**(1): 8−13.

Gonzalez S, Gupta J, Villa E, Mallawaarachchi I, Rodriguez M, Ramirez M, et al. 2016. Replication of genome-wide association study (GWAS) susceptibility loci in a Latino bipolar disorder cohort. *Bipolar Disorders*, **18**(6): 520−527.

Halbritter J, Bizet AA, Schmidts M, Porath JD, Braun DA, Gee HY, et al. 2013a. Defects in the IFT-B component IFT172 cause Jeune and Mainzer-Saldino syndromes in humans. American Society of Human Genetics, 93(5): 915-925.

Halbritter J, Porath JD, Diaz KA, Braun DA, Kohl S, Chaki M, et al. 2013b.

Identification of 99 novel mutations in a worldwide cohort of 1, 056 patients with a nephronophthisis-related ciliopathy. *Human Genetics*, **132**(8): 865−884.

Hamshere ML, Walters JTR, Smith R, Richards AL, Green E, Grozeva D, et al. 2013. Genome-wide significant associations in schizophrenia to *ITIH3/4, CACNA1C* and *SDCCAG8*, and extensive replication of associations reported by the Schizophrenia PGC. *Molecular Psychiatry*, **18**(6): 708−712.

Hartong DT, Berson EL, Dryja TP. 2006. Retinitis pigmentosa. *The Lancet*, **368**(9549): 1795−1809.

Hildebrandt F, Attanasio M, Otto E. 2009. Nephronophthisis: disease mechanisms of a ciliopathy. *Journal of the American Society of Nephrology*, **20**(1): 23−35.

Hsu PD, Lander ES, Zhang F. 2014. Development and applications of CRISPR-Cas9 for genome engineering. *Cell*, **157**(6): 1262−1278.

Hurd TW, Hildebrandt F. 2011. Mechanisms of nephronophthisis and related ciliopathies. *Nephron Experimental Nephrology*, **118**(1): e9−e14.

Insolera R, Shao W, Airik R, Hildebrandt F, Shi SH. 2014. SDCCAG8 regulates pericentriolar material recruitment and neuronal migration in the developing cortex. *Neuron*, **83**(4): 805−822.

Jiang L, Zhang HB, Dizhoor AM, Boye SE, Hauswirth WW, Frederick JM, et al. 2011. Long-term RNA interference gene therapy in a dominant retinitis pigmentosa mouse model. *Proceedings of the National Academy of Sciences of the United States of America*, **108**(45): 18476−18481.

Kang HG, Lee HK, Ahn YH, Joung JG, Nam J, Kim NKD, et al. 2016. Targeted exome sequencing resolves allelic and the genetic heterogeneity in the genetic diagnosis of nephronophthisis-related ciliopathy. *Experimental & Molecular Medicine*, **48**(8): e251.

Kenedy AA, Cohen KJ, Loveys DA, Kato GJ, Dang CV. 2003. Identification and characterization of the novel centrosome-associated protein CCCAP. *Gene*, **303**: 35−46.

Koenekoop RK, Cremers FPM, den Hollander AI. 2007. Leber congenital amaurosis: ciliary proteins on the move. *Ophthalmic Genetics*, **28**(3): 111−112.

Kumaran N, Moore AT, Weleber RG, Michaelides M. 2017. Leber congenital amaurosis/early-onset severe retinal dystrophy: clinical features, molecular genetics and therapeutic interventions. *British Journal of Ophthalmology*, **101**(9): 1147−1154.

May-Simera H, Nagel-Wolfrum K, Wolfrum U. 2017. Cilia – The sensory antennae in the eye. *Progress in Retinal and Eye Research*, **60**: 144−180.

Norris DP, Grimes DT. 2012. Mouse models of ciliopathies: the state of the art. *Disease Models & Mechanisms*, **5**(3): 299−312.

Otto EA, Hurd TW, Airik R, Chaki M, Zhou WB, Stoetzel C, et al. 2010. Candidate exome capture identifies mutation of *SDCCAG8* as the cause of a retinal-renal ciliopathy. *Nature Genetics*, **42**(10): 840−850.

Patil H, Tserentsoodol N, Saha A, Hao Y, Webb M, Ferreira PA. 2012. Selective loss of RPGRIP1-dependent ciliary targeting of NPHP4, RPGR and SDCCAG8 underlies the degeneration of photoreceptor neurons. *Cell Death & Disease*, **3**(7): e355.

Reiter JF, Leroux MR. 2017. Genes and molecular pathways underpinning ciliopathies. *Nature Reviews Molecular Cell Biology*, **18**(9): 533−547.

Rix S, Calmont A, Scambler PJ, Beales PL. 2011. An *Ift80* mouse model of short rib polydactyly syndromes shows defects in hedgehog signalling without loss or malformation of cilia. *Human Molecular Genetics*, **20**(7): 1306−1314.

Schaefer E, Zaloszyc A, Lauer J, Durand M, Stutzmann F, Perdomo-Trujillo Y, et al. 2011. Mutations in SDCCAG8/NPHP10 cause bardet-biedl syndrome and are associated with penetrant renal disease and absent polydactyly. *Molecular Syndromology*, **1**(6): 273−281.

Shamseldin HE, Shaheen R, Ewida N, Bubshait DK, Alkuraya H, Almardawi E, et al. 2020. The morbid genome of ciliopathies: an update. *Genetics in Medicine*, **22**(6): 1051−1060.

Stokman M, Lilien M, Knoers N. 2016. Nephronophthisis. *In*: Adam MP, Ardinger HH, Pagon RA, Wallace SE, Bean LJH, Gripp KW, et al. GeneReviews® [Internet]. Seattle: University of Washington .

Tay SA, Vincent AL. 2020. Senior-Løken syndrome and intracranial hypertension. *Ophthalmic Genetics*, **41**(4): 354−357.

Verbakel SK, van Huet RAC, Boon CJF, den Hollander AI, Collin RWJ, Klaver CCW, et al. 2018. Non-syndromic retinitis pigmentosa. *Progress in Retinal and Eye Research*, **66**: 157−186.

Watanabe Y, Fujinaga S, Sakuraya K, Morisada N, Nozu K, Iijima K. 2019. Rapidly Progressive Nephronophthisis in a 2-Year-Old Boy with a Homozygous SDCCAG8 Mutation. *Tohoku Journal of Experimental Medicine*, **249**(1): 29−32.

Weihbrecht K, Goar WA, Carter CS, Sheffield VC, Seo S. 2018. Genotypic and phenotypic characterization of the *Sdccag8*$^{Tn(sb\text{-}Tyr)2161B.\ CA1C2Ove}$ mouse model. *PLoS One*, **13**(2): e0192755.

Wright AF, Chakarova CF, Abd El-Aziz MM, Bhattacharya SS. 2010. Photoreceptor degeneration: genetic and mechanistic dissection of a complex trait. *Nature Reviews Genetics*, **11**(4): 273−284.

Yamamura T, Morisada N, Nozu K, Minamikawa S, Ishimori S, Toyoshima D, et al. 2017. Rare renal ciliopathies in non-consanguineous families that were identified by targeted resequencing. *Clinical and Experimental Nephrology*, **21**(1): 136−142.

Zaghloul NA, Katsanis N. 2009. Mechanistic insights into Bardet-Biedl syndrome, a model ciliopathy. *The Journal of Clinical Investigation*, **119**(3): 428−437.